How to Cite: Ergashev, K.Kh., Vokhidova, N.R., & Rashidova, S.Sh. (2026). Synthesis of Stabilized Manganese-Containing Nanoparticles with *Bombyx mori* Chitosan Macromolecules under *In Situ* Conditions. *Eurasian Journal of Chemistry, 31, 1(121), 8–29.* https://doi.org/10.31489/2959-0663/1-26-1

ADVANCED POLYMERS AND NANOMATERIALS FOR DRUG DELIVERY AND OTHER BIOMEDICAL APPLICATIONS

Article

Received: 21 November 2025 | Revised: 23 February 2026 | Accepted: 2 March 2026 | Published online: 10 March 2026

UDC 541.64: 547.458.61:544.773

https://doi.org/10.31489/2959-0663/1-26-1

Kandiyor Kh. Ergashev*, Noira R. Vokhidova, Sayyora Sh. Rashidova

Institute of Polymer Chemistry and Physics, Tashkent, Uzbekistan
*(*Corresponding author's e-mail: kandiyor_ergashev@yahoo.com)*

Synthesis of Stabilized Manganese-Containing Nanoparticles with *Bombyx mori* Chitosan Macromolecules under *In Situ* Conditions

Manganese nanoparticles are highly reactive and tend to aggregate and oxidize, which limits their practical application. Therefore, the aim of this study was to synthesize and stabilize Mn nanoparticles using *Bombyx mori* chitosan as a natural biopolymer matrix under controlled *in situ* conditions and to investigate their structural and physicochemical properties. Samples containing Mn nanoparticles stabilized with chitosan in the presence of reducing agents, with hydrodynamic dimensions of 118 nm (97 %) and 144 nm (96 %), were synthesized under *in situ* conditions. The structural and morphological characteristics were studied using IR spectroscopy, X-ray diffraction (XRD), dynamic light scattering (DLS), and electron microscopy. IR spectroscopic studies revealed local rearrangements within the repeating units of the chitosan polymer chain and interactions between the –NH and –C=O functional groups and manganese-containing nanoparticles. XRD analysis confirmed the reduction of Mn^{2+} ions. Morphological studies of chitosan–manganese films showed the formation of 50 nm tetragonal and 90 nm spherical metal nanoparticles under the selected synthesis conditions. The results confirm the stabilization of Mn nanoparticles with *Bombyx mori* chitosan by the chemisorption method and demonstrate effective control of particle size and morphology. Further research should focus on evaluating long-term stability, functional properties, and potential biomedical applications of the synthesized nanocomposites.

Keywords: manganese nanoparticles, chitosan, *Bombyx mori*, nanocomposites, *in situ* synthesis, chemisorption, biopolymers, nanoparticle stabilization, particle morphology, size control

Introduction

Manganese (Mn) is an essential trace element for the body, providing enzyme activity, antioxidant protection, and hormonal balance. The role of this element in the reproductive system has been the focus of attention in recent years, and its effects can be positive or negative depending on the dose [1–3]. Manganese plays a crucial role in antioxidant protection, particularly by stimulating the activity of superoxide dismutase (Mn-SOD), which reduces oxidative stress in spermatozoa and oocytes [1, 4]. Additionally, Mn enhances energy metabolism, particularly glycolysis, and promotes follicle development in granulosa and oocyte cells [5, 6]. Manganese activates enzymes involved in the synthesis of cholesterol-based hormones (testosterone, progesterone). In this way, it regulates the secretion of FSH (Follicle-Stimulating Hormone) and LH (Luteinizing Hormone), thereby maintaining hormonal balance through the hypothalamic-pituitary-ovarian axis [7, 8]. High doses of manganese reduce sperm count and motility, lower testosterone levels, and can minimize ovarian mass by up to 25–30 % [8, 9]. These effects are dose-dependent and show a U-shaped

dose-response relationship [10]. Manganese enhances the glycolysis pathway in granulosa cells, increasing the expression of the enzymes GLUT4 (*Glucose Transporter Type 4*) and PFKL (*Phosphofructokinase, Liver Type*) [5]. This activates the mTOR (mechanistic *Target of Rapamycin*) and PI3K/Akt (*Phosphoinositide 3-Kinase / Protein Kinase B (Akt)*) signaling cascades, which stimulate follicular development [10, 11].

In addition, it can also affect the ovulatory process through the IGF1 (Insulin-like Growth Factor 1)/mTOR signaling cascade, kisspeptin expression, and gene regulation [12, 13]. Manganese is an essential trace element for the reproductive system, and while it is beneficial at moderate doses, it can be toxic at high doses. Recent studies have focused on uncovering the precise molecular mechanisms of these effects, which could provide a solid basis for clinical studies [14]. The dual effects of manganese on reproductive health and its high dose sensitivity highlight the need for its delivery in a bioavailable, stable, and controlled form. In this regard, the synthesis of manganese in nanoparticle form is a crucial scientific direction for the development of targeted therapeutic applications in the reproductive system, as it enhances its bioavailability, tissue specificity, and pharmacokinetic properties.

The methods used to synthesize manganese nanoparticles determine the size, shape, degree of crystallinity, and function of the particle. There are various methods for synthesizing manganese (Mn) nanoparticles, each with its own advantages and disadvantages. One of the traditional methods, the co-precipitation method, is simple, inexpensive, and allows for the obtaining of large quantities of nanoparticles; however, it is difficult to precisely control the particle size, and the possibility of agglomeration is high [15]. Hydrothermal and solvothermal methods enable the formation of crystal structures under high temperatures and pressures. In the hydrothermal method, water serves as the primary medium, whereas in the solvothermal method, organic solvents are the primary medium. The advantages of this method are high phase purity and easy control of shape and size [16, 17]. One of the modern methods, "green synthesis", converts Mn salts into nanoparticles using plant extracts (phytochemicals such as flavonoids and polyphenols). It is also possible to oxidize Mn^{2+} using microorganisms (some bacteria and fungi) to produce bio-nanoparticles. The green synthesis method is environmentally friendly, convenient, and inexpensive; however, the reaction time is long, and scaling up presents difficulties [18, 19]. Additionally, microwave and ultrasonic (sonochemical) synthesis methods offer energy-efficient and rapid reaction conditions. In the microwave method, the reaction is heated uniformly and quickly. In ultrasonic synthesis, the particles are crushed due to the cavitation effect [20]. Today, manganese ferrite nanoparticles ($MnFe_2O_4$) are used in magnetic materials (MRI), sensors, catalytic, and environmental purification technologies. Co-precipitation, sol-gel, microwave, and "combined" methods are mainly used for their synthesis [21].

However, it should be noted that these methods have primarily synthesized nanoparticles of manganese oxides, such as MnO, MnO_2, α-MnO_2, β-MnO_2, and Mn_3O_4. The synthesis of elemental manganese (Mn^0) nanoparticles remains a significant challenge and is relatively poorly understood in the scientific literature. Several factors can be identified as the primary issues in the synthesis. Since manganese atoms show a high affinity (oxophily) for oxygen, it isn't easy to stably maintain and synthesize its elemental state (Mn^0).

Manganese is rapidly oxidized upon exposure to air, forming oxide phases such as MnO, Mn_3O_4, and MnO_2 [22]. Even when synthesized in an inert environment, the formation of an oxidized layer is likely to occur [23]. Potent reducing agents are required to obtain Mn from manganese salts. However, these substances (e.g., $NaBH_4$, H_2, $LiAlH_4$) are highly reactive, hazardous to handle, and difficult to control. Additionally, even under these chemical reduction conditions, the particles are not completely reduced, and mixed phases (Mn/MnO and Mn_3O_4) are formed [24]. Synthesized manganese nanoparticles are prone to agglomeration and lose their uniformity in size and shape. This negatively affects their catalytic, optical, and magnetic properties [25]. Due to their high density, they are not stable in suspension in water or organic media [26].

Most scientific research has focused on the study of the oxide forms of manganese (MnO, MnO_2, Mn_3O_4), and not enough attention has been paid to elemental Mn particles. According to a literature review, the number of articles on Mn^0 nanoparticles published over the last 10 years is minimal, and even those that have been published have primarily been in the context of catalysis or nanocomposites [22, 27].

Recent studies have demonstrated that stable Mn nanoparticles can be synthesized under inert atmospheres (Ar, N_2) using microwave energy [23, 28]. Another promising approach is to protect manganese particles from oxidation by coating them with organic ligands or polymers. For example, the use of stabilizers based on oleyl amine, polyethylene glycol, or cellulose can ensure the stability of Mn in air [25, 26]. Therefore, this work aims to synthesize stabilized Mn in the presence of *Bombyx mori* chitosan

(CS), which has stabilizing properties, to overcome the problems associated with the oxidation susceptibility and agglomeration of manganese nanoparticles.

Experimental

Chemicals and Materials

For the research work, *Bombyx mori* chitosan (molecular mass 41×10^3 Da; deacetylation degree 86 %), $MnCl_2\cdot4H_2O$ with a purity of ≥ 99.0 % (Shanghai Aladdin Biochemical Technology Co., Ltd.), $NaBH_4$ with a purity of 98 % (Sinopharm Chemical Reagent Co., Ltd.), and mild reducing agent $C_6H_8O_6$ (Macklin Biochemical Co., Ltd.) were used. All reagents were of "analytical grade" grade, with a purity of ≥99.0 %, and were used without additional purification procedures. All solutions were prepared in deionized water.

Infrared Spectroscopy (FTIR) Analysis

IR spectroscopic analysis was performed on a Bruker INVENIO-S-S model (in the range of 400–4000 cm^{-1}). The samples were prepared in the form of tablets in the presence of potassium bromide (KBr) salt. FTIR spectra of chitosan and chitosan-stabilized Mn nanosystems were recorded for characterization of their functional groups [29–31].

X-Ray Diffraction (XRD)

The phase composition and crystallinity of the samples were investigated using a DRON-3M X-ray diffractometer under Co Kα radiation (U = 22 kV, I = 16 mA). The crystallite size was calculated using the Debye-Scherrer equation (K = 0.9; β — FWHM; RD patterns were recorded using Co Kα radiation (λ = 1.7902 Å).). The degree of crystallization was determined by the ratio of the intensities of J (crystalline peak) and J_a (amorphous background) [32].

Atomic Force Microscopy (AFM)

The morphological characteristics of the samples were analyzed using atomic force microscopy (Agilent 5500, USA). Silicon cantilevers ($k \approx 9.5$ N/m; resonant frequency ≈ 145 kHz) were used. The scanning area was 15×15 μm^2 in the X and Y axes, and ≈ approximately one μm in the Z axis. Images were acquired at 22 °C in tapping mode. The average particle size and distribution were estimated by histogram analysis.

Scanning Electron Microscopy (SEM) and Energy Dispersive Spectroscopy (EDS)

The surface morphology of the samples was studied using a JEOL JSM–IT210 scanning electron microscope. The operating voltage ranged from 5 to 15 kV, and the working distance was ≈ approximately 10.8 mm. Images at various scales were obtained using the InTouchScope software. Energy dispersive spectroscopy (EDS) analyses were performed to determine the elemental composition. The content of carbon (C), nitrogen (N), oxygen (O), and manganese (Mn) was noted; silicon (Si) peaks were explained by the effect of the glass substrate (SiO_2).

Synthesis of Mn Particles without Polymer Matrix (Control Experiment S-1, S-2)

In the control experiment (without chitosan), 20 ml of a 0.0012 mol/L solution of $MnCl_2$ was used. The reaction was carried out at 30 °C with intensive stirring at 600 rpm. A 0.025 mol/L solution of $NaBH_4$ was added dropwise to this system.

The main reduction reaction takes place in the following form [33, 34]:

$$MnCl_2 + 2NaBH_4 + 6H_2O \rightarrow Mn(s) + 2NaCl + 2B(OH)_3 + 7H_2\uparrow$$

In sample S-1, only $NaBH_4$ was used as a reducing agent.

In sample S-2, ascorbic acid ($C_6H_8O_6$, 3.5×10^{-5} mol/L) was added together with $NaBH_4$ [33–38]:

$$MnCl_2 + NaBH_4 + C_6H_8O_6 \rightarrow Mn + NaCl + H_2 + B(OCH_2)_3 + \\ + \text{(Mn-borate complex and similar by-products)}$$

$NaBH_4$, as a potent reducing agent, quickly reduces Mn^{2+} ions to the Mn state. In contrast, ascorbic acid, as a relatively mild reducing agent, controls the kinetics of particle growth, limits agglomeration, and ensures the stability of the resulting suspension [39–41].

Synthesis of Mn Nanoparticles under in situ Conditions (S-3, S-4)

In the *in situ* synthesis process, a chitosan solution (0.06 mol/L) was added to the reaction medium prior to the commencement of the reaction. Then, a 0.0012 mol/L $MnCl_2$ solution was stirred at 30 °C and 600 rpm, and a 0.025 mol/L $NaBH_4$ solution was added dropwise. In sample S-3, only $NaBH_4$ was used as a reducing agent. In sample S-4, ascorbic acid (3.5×10^{-5} mol/L) was added along with $NaBH_4$. The polycationic nature of chitosan creates an electrostatic barrier around the particle core, thereby limiting the growth and agglomeration of the core. Thus, chitosan enhances the colloidal stability of the suspension, ensures the hydrophilicity of the resulting nanoparticles, and facilitates their uniform size distribution [42–44].

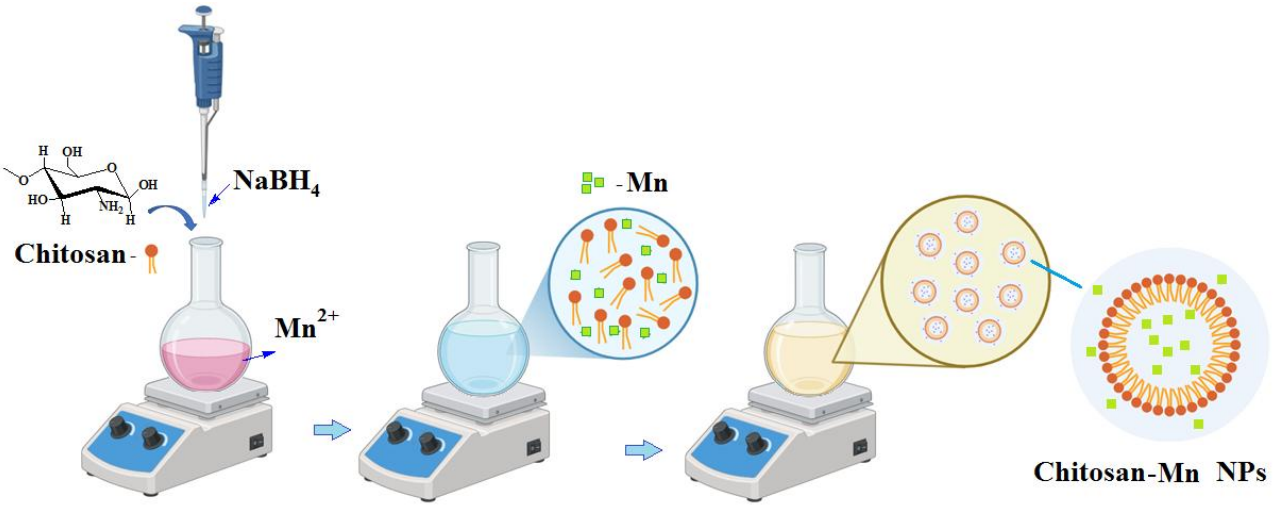

a) Synthesis of CS-Mn nanoparticles in the presence of $NaBH_4$ reducing agent under *in situ* conditions

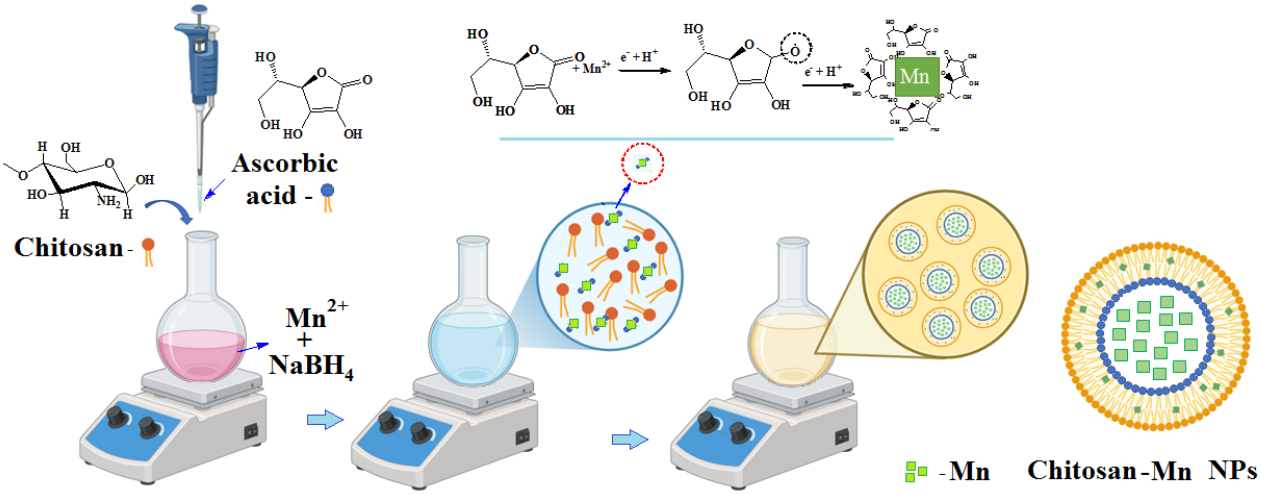

b) Synthesis of CS-Mn nanoparticles in the presence of $NaBH_4/C_6H_8O_6$ reducing agent under *in situ* conditions

Figure 1. Synthesis of CS-Mn nanoparticles under *in situ* conditions
Illustration created in BioRender. Ergashev, Q. (2026) https://BioRender.com/qy5h0tq

The chitosan/Mn suspensions obtained after synthesis were purified from excess ions and small molecules by dialysis. For this purpose, a cellulose acetate membrane was used (nominal cutoff size ≈500 nm). The dialysis process was carried out for 24 hours, with the dialysis water being replaced every 3 to 4 hours. This effectively cleared the colloidal system of excess salts and reaction products [29].

Dynamic Light Scattering (DLS) Analysis

DLS determined the hydrodynamic size and distribution of the particles, and the analysis was performed using a Photocor Compact spectrometer with a He-Ne laser source at a wavelength of 632.8 nm. The samples were prepared in an aqueous medium and stored at a thermostated temperature of 25 °C ± 0.1 °C. The sample concentration was maintained at 0.05 mg/mL, a low level designed to prevent

aggregation. Each sample was measured for 3 minutes in at least three replicates. The particle size range was determined to be between 1 nm and 100 μm. DLS analysis was primarily employed to evaluate the hydrodynamic size distribution of nanoparticles and to assess the influence of chitosan on particle size control.

Statistical Analysis

All experiments were repeated at least three times ($n = 3$), and the results are presented as mean ± standard deviation (SD). The Shapiro–Wilk test was used to test the hypothesis of normal distribution. Differences between groups were tested by one-way ANOVA*; when significant differences were noted, Tukey's post hoc test was used. All calculations and graphs were performed using OriginPro 2023 (OriginLab, USA) and GraphPad Prism 9.0 (GraphPad Software, USA). The significance level in all statistical tests was set at $p < 0.05$.

Results and Discussion

Hydrodynamic Sizes (DLS Analyses)

Dynamic light scattering (DLS) analysis of the chitosan solution (CS) showed a broad number-weighted hydrodynamic size distribution with an average size in the range of approximately 3–4 μm, indicating a polydisperse system with a dominant population in the micrometer range.

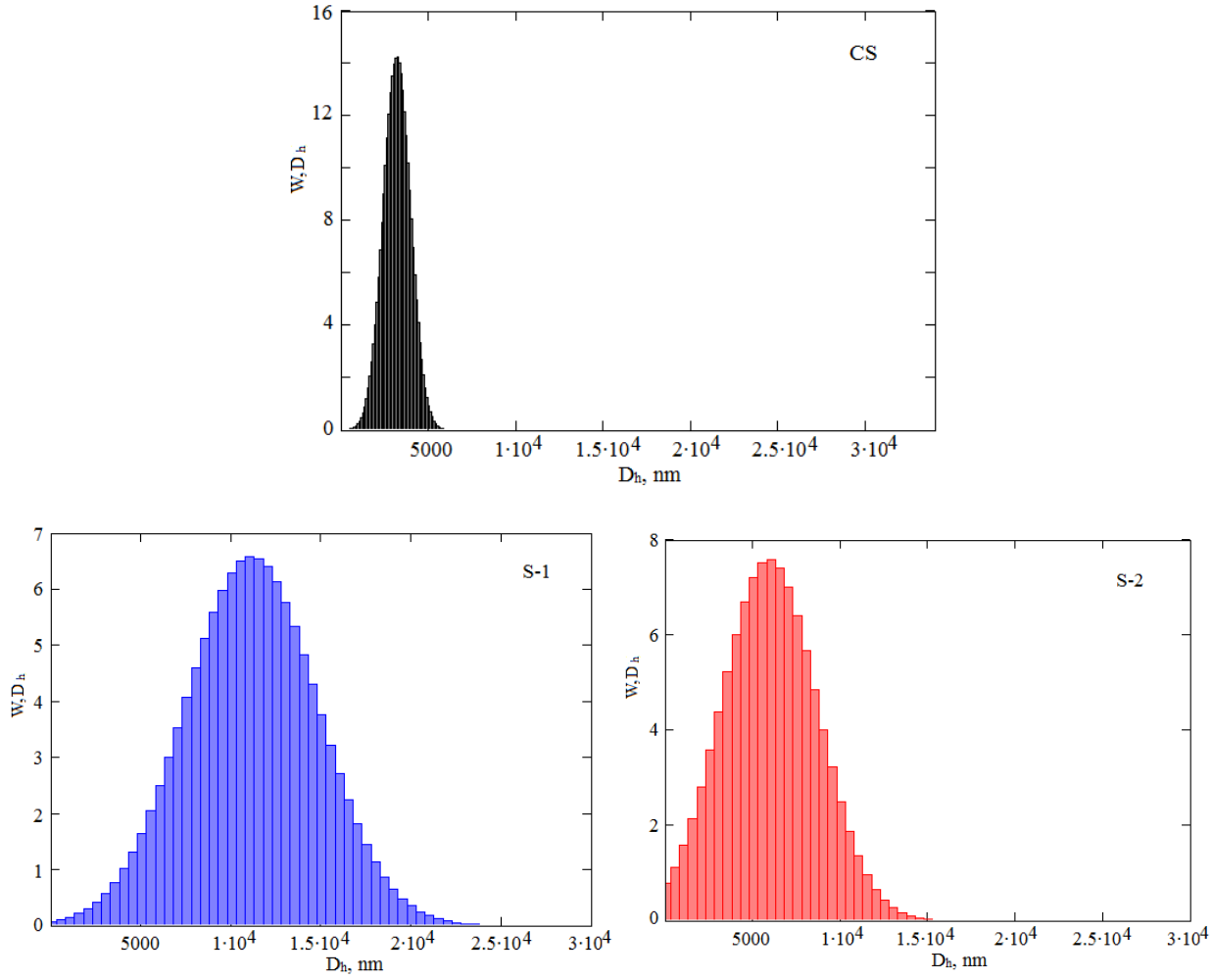

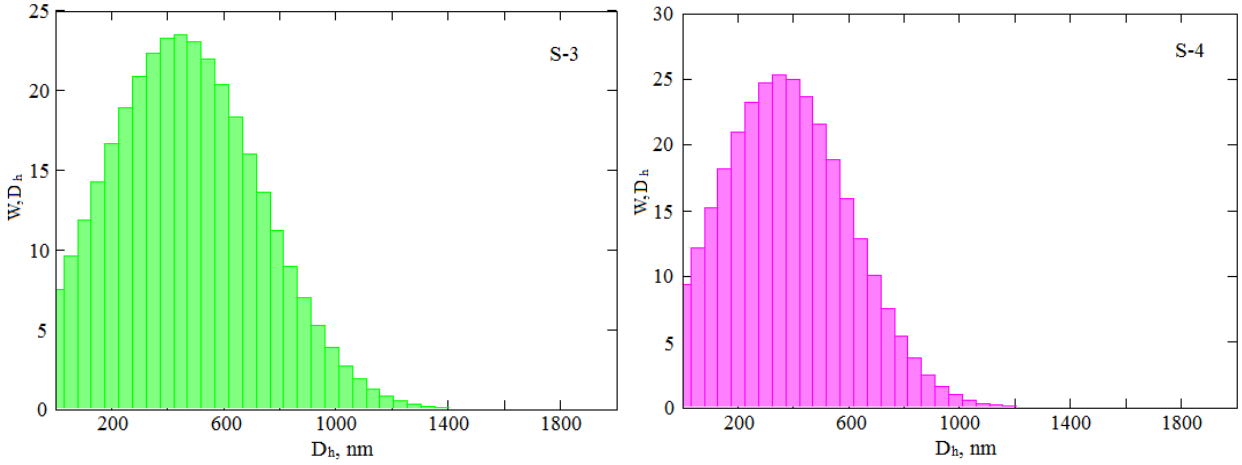

Figure 2. Hydrodynamic radius distributions of manganese-containing particles obtained under control conditions without polymer matrix (S-1, S-2) and by *in situ* synthesis in the presence of chitosan (S-3, S-4)

The results indicate that, in the control experiments performed in the absence of chitosan, DLS analysis revealed apparent hydrodynamic sizes predominantly in the micrometer range. Specifically, the S-1 sample exhibited a single broad population with an average hydrodynamic size of approximately 10–12 μm. In contrast, the S-2 sample showed a dominant population with average hydrodynamic sizes in the range of 6–8 μm (Fig. 2). It should be emphasized that such micrometer-scale DLS signals are most likely associated with pronounced particle aggregation and partial sedimentation occurring in the absence of a stabilizing polymer matrix, rather than with the presence of stable primary nanoparticles. The strong reducing capability of $NaBH_4$ promotes rapid reduction of Mn^{2+} ions, resulting in uncontrolled nucleation and extensive aggregation. In contrast, the use of ascorbic acid as a weaker reducing agent (S-2) leads to slower nucleation, allowing the transient formation of smaller species prior to aggregation, in agreement with previously reported studies [45–47].

The hydrodynamic size distributions of manganese-containing particles obtained via *in situ* synthesis in the presence of chitosan revealed a dominant nanoscale population. For both samples S-3 and S-4, the average hydrodynamic particle sizes were found to be in the range of approximately 300–500 nm (Fig. 2). In comparison with the control experiments, this shift toward smaller and more uniform sizes indicates a moderated nucleation–growth process. Such behavior reflects the stabilizing influence of chitosan on manganese-containing particles formed under *in situ* synthesis conditions, leading to reduced aggregation and a more controlled particle size distribution [38, 40-41, 46].

IR-Spectroscopic Analysis

In the IR spectrum of the original chitosan, characteristic absorption bands corresponding to the macromolecule were observed. In particular, a broad band in the range of 3400–3450 cm^{-1} is characteristic of stretching vibrations of the –OH and $–NH_2$ groups, which has a relatively broad appearance due to the strong N–N bonds in chitosan molecules. The peaks at 2920–2930 cm^{-1} and 2850 cm^{-1} correspond to asymmetric and symmetric C–H stretching vibrations of the $–CH_2$ and –CH groups. The peak in the range of 1650–1660 cm^{-1} (Amid I) mainly refers to stretching vibrations of the C=O bond. The peak in the region of 1560–1580 cm^{-1} is associated with deformation vibrations of the N–H bond (Amid II). The peaks at 1410–1430 cm^{-1} and 1375 cm^{-1} represent the stretching and bending vibrations of the $–CH_2$ and $–CH_3$ groups, respectively. The band observed between 1150–1070 cm^{-1} is assigned to asymmetric C–O–C glycosidic stretching vibrations of chitosan (Fig. 3, 1) [42–44].

It is well established from the literature that, upon interaction with various metals and their oxides, chitosan exhibits adsorption on its surface through its –OH and $–NH_2$ functional groups. This process is mainly ensured by hydrogen bonds, electrostatic interactions, and polymer-matrix structure [45]. In the IR spectrum of the S-3 composite formed by chitosan with manganese nanoparticles, shifts in the vibration peaks of the amine and amide groups were observed at ~1544 cm^{-1} → ~1636 cm^{-1} and ~1402 cm^{-1} → ~1374 cm^{-1} (Fig. 3, 2). This indicates the electrostatic interaction of $–NH_2$ and C–N groups with Mn particles on the surface [43, 45]. In some cases, the amide I/II peaks shifted from 1647 cm^{-1} to ~1560 cm^{-1}, indicating donor-acceptor interactions through the –C=O and $–NH_2$ groups.

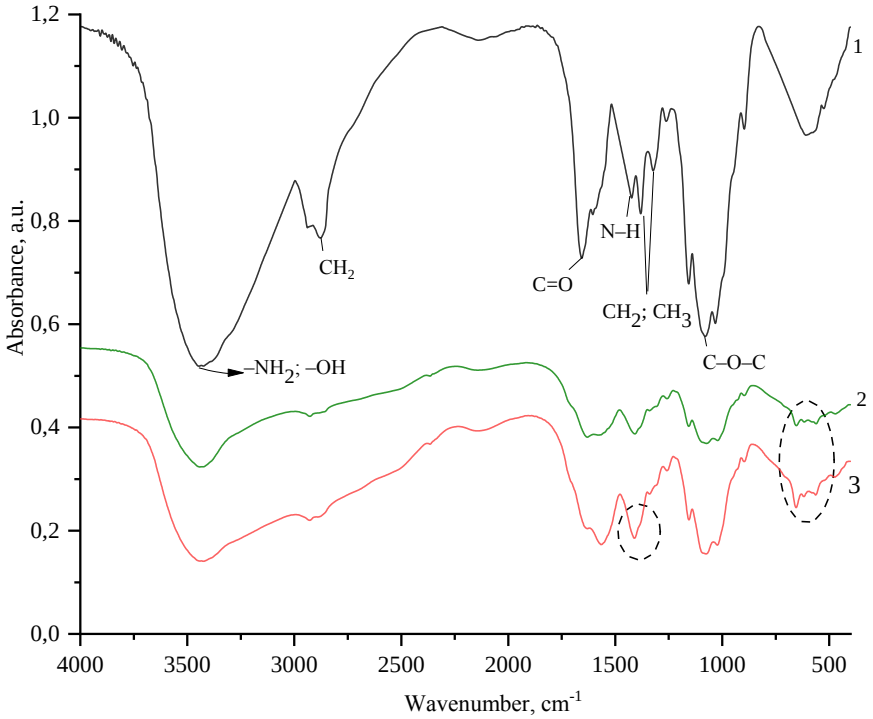

Figure 3. IR spectrum of chitosan (*1*), S-3 (*2*), and S-4 (*3*) samples

The peaks in the range of 1155, 1073, and 1021 cm^{-1}, characteristic of C–O–C glycosidic bonds, are largely preserved. However, the decrease in intensity at 1258 cm^{-1} may indicate the possibility of non-covalent interactions of the Mn–OH or Mn–OH type through hydroxyl groups. These results are consistent with the literature [47]. Additionally, the shift of the CH_2/CH_3 vibration peaks from 1423 cm^{-1} to 1383 cm^{-1} is attributed to local structural changes in the polymer environment. Although manganese NPs are not oxidized, they exhibit metal-polymer surface interactions through weak but consistent peaks around ~560–600 cm^{-1} in the IR spectrum [48-49]. These peaks are due to the metal interacting with –OH and $–NH_2$ groups through surface activity.

The IR spectrum of the S-4 sample, shows shifts in the –N–H and –C=O vibrational bands associated with $–NH_2$, C=O, and C–N (amide) groups, indicating the presence of intermolecular hydrogen bonding or electrostatic interactions between chitosan and manganese species.The shift of the peaks belonging to the CH_3/CH_2 and C–O groups indicated that these structural units participate in the stabilization of the nanoparticles within the matrix through peripheral adsorption (Fig. 3, 3) [50–52]. The new peak appearing at 895 cm^{-1} can be interpreted as a local geometric rearrangement in the chitosan skeleton or a metal-hydroxyl (Mn–OH) bond. Peaks in the range of 654–617–562 cm^{-1} indicate the strength of Mn–O or Mn–OH bonds, suggesting a “tunnel-like” arrangement of nanoparticles within chitosan. Although ascorbic acid is involved in the formation, IR results indicate that it does not directly react chemically with chitosan, but instead acts physically, i.e., as a passive stabilizer [50–54].

XRD Analysis

The phase structures of chitosan and its stabilized S-3 and S-4 samples were studied by X-ray diffraction analysis. The crystalline structure of chitosan is in a semi-amorphous state, which shows two prominent diffraction peaks: 2θ = 10.49° (020) (amid I “$–N–CO–CH_3$”) and 19.95° (110) (amid II “$–NH_2$”) (Fig. 4) [55, 56, 57].

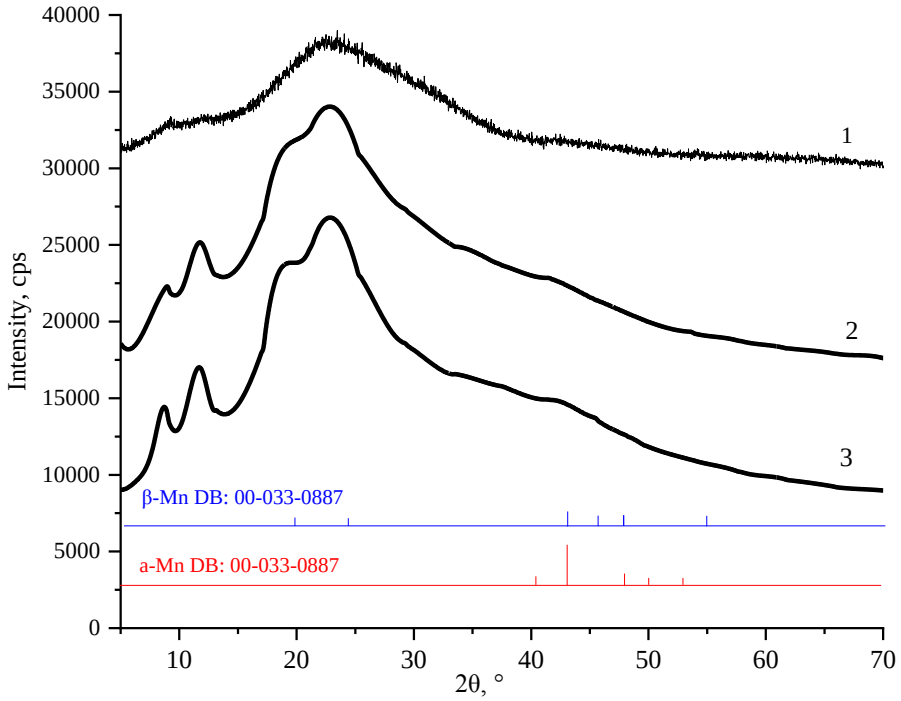

Figure 4. XRD patterns of chitosan (*1*), S-3 (*2*), and S-4 (*3*) samples

Manganese is a 3d-metal with various allotropic forms. Its main crystalline phases, α-Mn and β-Mn, are distinguished by their atomic structure, thermodynamic stability, and X-ray diffraction characteristics. Based on XRD analyses of these phases in the literature, the prominent diffraction peaks for α-Mn are located in the following positions in Cu Kα light: 2θ 38.5°, 44.8°, 65.1°. These peaks correspond to the (220), (311), (400) orientations, respectively [58]. The β-Mn phase is stable at high temperatures (T > 973 K) and has a cubic (chiral) structure [59, 60]. The prominent simulated XRD peaks for the β-Mn phase are: 2θ 38.5°; 44.8°; 65.1°; 78°, 82° and these peaks are mainly associated with the (220), (311), and (400) bonds [61, 62].

The diffraction peaks and crystal parameters of the S-3 and S-4 samples, as determined by XRD analysis, are presented in Table 1.

Table 1

Crystal parameters and crystal sizes of chitosan, S-3, and S-4 samples

No.	2θ, °	d, Å	(FWHM) β, °	(Size) L, Å	Crystallinity, %
CS					
1	10.49	8.43	2.54	3.28	38
2	19.95	4.44	1.98	4.3	
Sample S-3					
3	8.53	10.36	1.36	61	53
4	11.73	7.53	2.38	35.0	
5	18.26	4.85	2.51	33.4	
6	21.78	4.07	7.97	10.60	
7	43.63	2.07	6.4	14.1	
Sample S-4					
8	8.49	10.41	1.91	43.5	48
9	11.58	7.64	2.37	35.1	
10	18.48	4.79	2.5	34	
11	21.94	4.04	7.49	11.28	
12	43.40	2.08	5.3	16.9	
13	60.5	1.52	9	11	

In the XRD pattern of sample S-3, 2θ 8.53°, 11.73°, 18.26°, and 21.78° are the peaks that are shifted due to the interaction of chitosan with Mn nanoparticles. These peaks are due to structural rearrangement, interaction of manganese nanoparticles with chitosan chains through electrostatic and hydrogen bonding, and these interactions disrupt the ordered arrangement between chitosan molecules, causing a shift in the position of the diffraction peaks [63]. Such peaks have also been observed in chitosan–metal oxide composites [64]. The 2θ 43.63° peak indicates that the Mn^0 metallic state is stable in the nanoparticles, which is mainly reflected on the (111) crystal surface [65–67]. The composition of sample S-3 produced CS/Mn crystal types consisting of α-Mn cubic (*a* — 5.218, *b* — 5.218, *c* — 5.218 Å), β-Mn cubic (*a* — 4.433, *b* — 4.433, *c* — 4.433 Å) and tetragonal structure (*a* — 10.784, *b* — 11.329, *c* — 4.449 Å) was determined to be.

In the XRD pattern of sample S-4, the peaks at 2θ 8.53° (020) and 11.73° (110) are shifts of the 10.49° peak in pure chitosan. The peaks at 2θ 18.26° and 21.78° are shifts of the 19.95° peak in pure chitosan. The reasons for these shifts have been explained above [63, 64]. Ascorbic acid changes the hydrogen bonds between water molecules and hydroxyl groups in the chains, causing local disorder. It is also possible that after these Mn nanoparticles enter the chitosan matrix, local disorders occur in the order of the molecular chains, which leads to broadening and shifting of the peaks [68]. The peak at 2θ 43.63° (111) belongs to the crystalline phase of metallic manganese (Mn). Ascorbic acid more effectively chemically reduced Mn^{2+} ions to the Mn state, and manganese nanoparticles were formed with a high degree of crystallinity. In addition, a new 2θ 60.5° peak was formed in sample S-4. This peak was based on metal–carboxyl or metal–amine bonds, and it was noted that a new crystal or quasi-crystalline structure was formed in the composite structure, or that metal complexes of chitosan in the sources gave a peak around 2θ ≈ 60°. It was found that the composition of sample S-4 was α-Mn cubic (*a* — 5.218, *b* — 5.218, *c* — 5.218 Å), β-Mn cubic (*a* — 4.433, *b* — 4.433, *c* — 4.433 Å) and the formation of new crystal types of the CS-Mn system with a tetragonal structure (*a* — 11.81, *b* — 7.860, *c* — 4.072 Å). The results obtained in the S-5 sample show that ascorbic acid, as a reducing agent in the reaction, converts Mn^{2+} ions to the Mn state and interacts with chitosan chains, changing their molecular order [69, 70].

It should be noted that the diffraction peak observed at 2θ ≈ 43° cannot be considered unambiguous evidence of the presence of Mn alone, as this region may overlap with reflections of MnO, Mn_3O_4, or mixed manganese-containing phases. Furthermore, IR spectroscopy does not allow a clear distinction to be made between metallic manganese and its oxide compounds. Given the aqueous synthesis conditions and exposure to air, partial oxidation of the surface of the Mn nanoparticles or the formation of mixed Mn/Mn_xO_y nanostructures cannot be ruled out. Similar surface oxidation phenomena have been widely described for manganese-containing nanoparticles synthesized in polymer matrices [63, 64, 68–70]. Therefore, the resulting nanoparticles are more accurately described as manganese-containing nanoparticles, potentially consisting of a metal core with an oxidized surface layer.

AFM Analysis

AFM analyses show that chitosan films often have a rough, granular or cross-linked morphology. This is dependent on the molecular weight and degree of deacetylation of chitosan. For example, it has been reported that a decrease in the molecular weight of chitosan leads to the formation of small blocks on the surface and a decrease in crystallinity [71]. The surface morphology and particle distribution of chitosan films were analyzed by atomic force microscopy (AFM). The results of 3D topography showed that the surface of the chitosan film is not uniform, but is characterized by a globular morphology. The maximum value of the vertical relief (*Z*-axis) is on average around 360 nm, which is associated with the predominantly amorphous structure of the chitosan chains and the formation of surface defects (Fig. 5). Such rough surface morphology has been noted in AFM studies as a characteristic of the natural polysaccharide nature of chitosan [72-73].

Histogram analysis revealed that the average particle size was 0.308 μm and that they were mainly distributed in the range of 0.154–0.462 μm. These parameters indicate that the chitosan film is homogeneous at the nanoscale and consists of globular structures. The presence of chitosan particles in nanometers can enhance its sorption capacity and have a positive effect on the process of complex formation with metal ions, the formation of nanostructures with various morphologies with metals [71–73]. It can be seen that the particles with a relief pattern height of 100–200 nm on the surface formed a heterogeneous surface.

In order to fully study the morphological structure of the chitosan-Mn-based nanosystem, AFM images were obtained. The AFM image of sample S-3 confirmed the XRD and SEM results and showed that it consists of nanoparticles with a cubic and tetragonal structure. The formed nanoparticles formed

agglomerates densely located and less than 1 μm in size. The particle distribution histogram with respect to the surface is asymmetric, with nanoparticles distributed in the range from 10 nm to 110 nm, with an average size of 50 nm accounting for 14 %. It can be seen that the distribution of Mn nanoparticles along the polymer matrix on the surface of the film is not uniform on the uneven surface (Fig. 6).

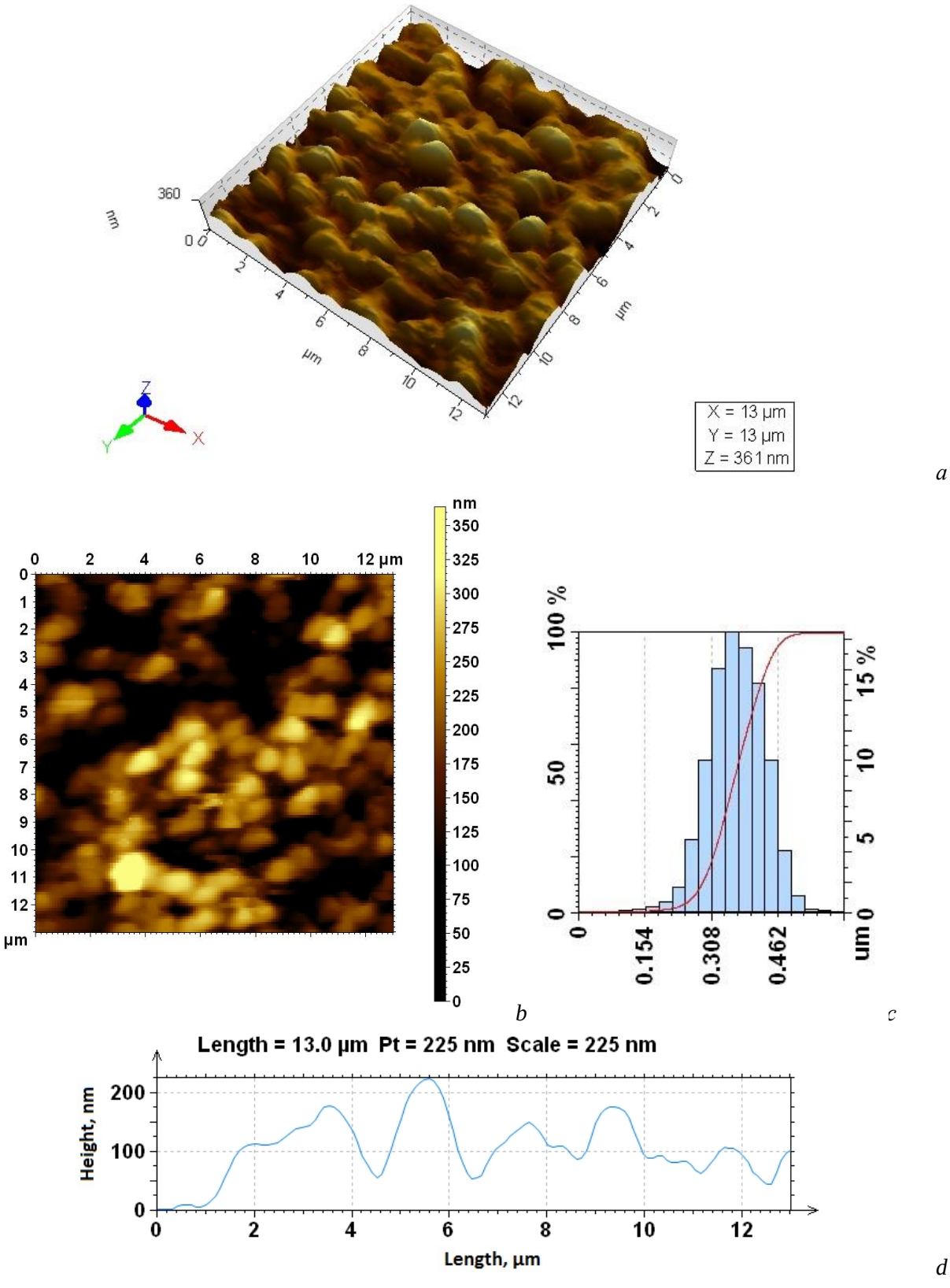

Figure. 5. AFM image (*a*, *b*), distribution histogram (*c*) and surface relief (*d*) of a *Bombyx mori* chitosan film

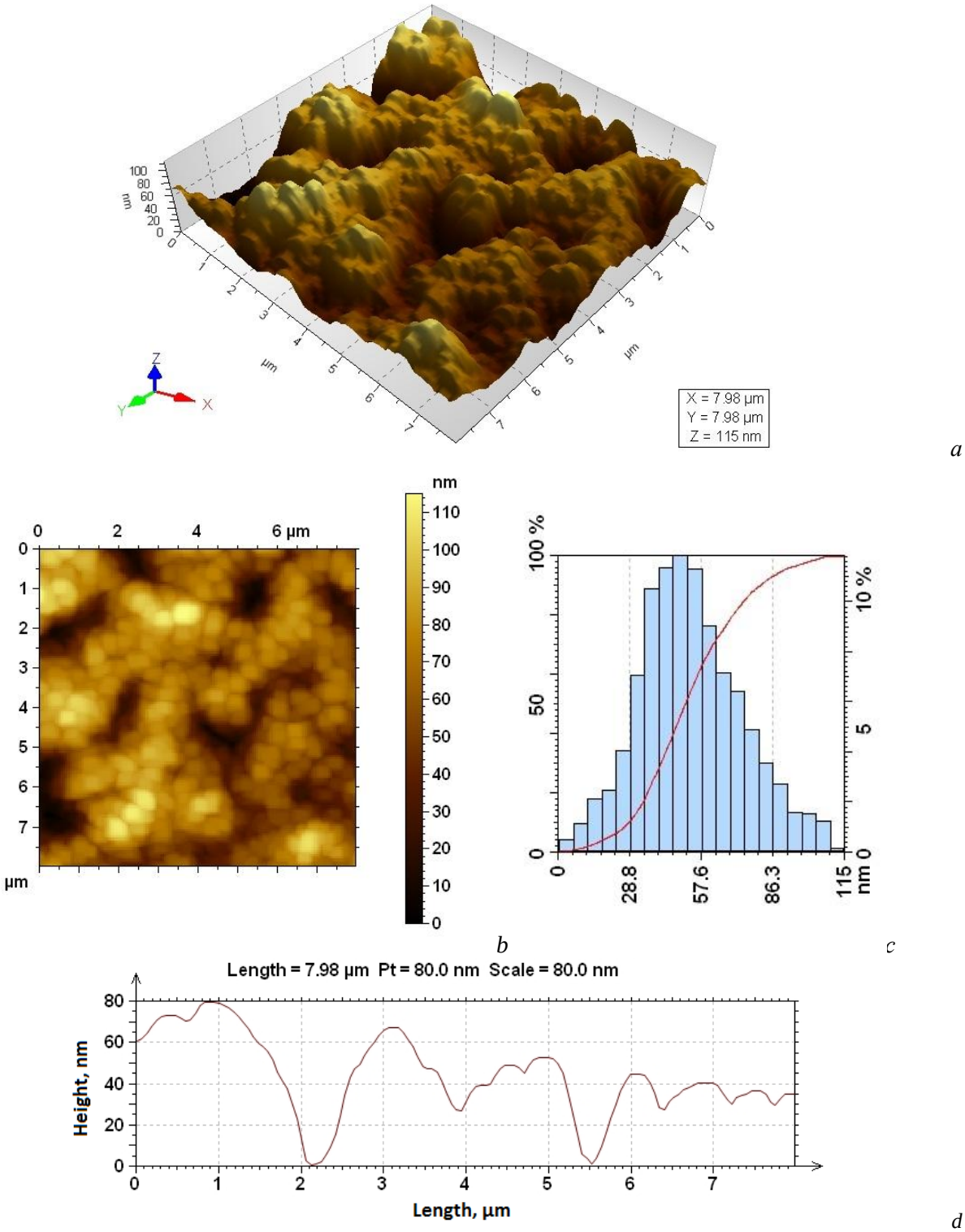

Figure 6. AFM image (*a*, *b*), distribution histogram (*c*) and surface relief (*d*) of the film of sample S-3 (in the presence of $NaBH_4$)

In the AFM image of the S-4 sample, the NPs are more sparsely distributed in the chitosan matrix compared to the S-3 sample, and the number of larger agglomerates is also less. The particle distribution histogram with respect to the surface is also asymmetric in the S-4 sample, with the nanoparticles having sizes in the shorter range from 50 to 100 nm, with an average of 40 % of the nanoparticles being 90 nm. The film surface is smoother than that of the S-4 sample, but the distribution of Mn NPs along the chitosan matrix is unevenly distributed (Fig. 7).

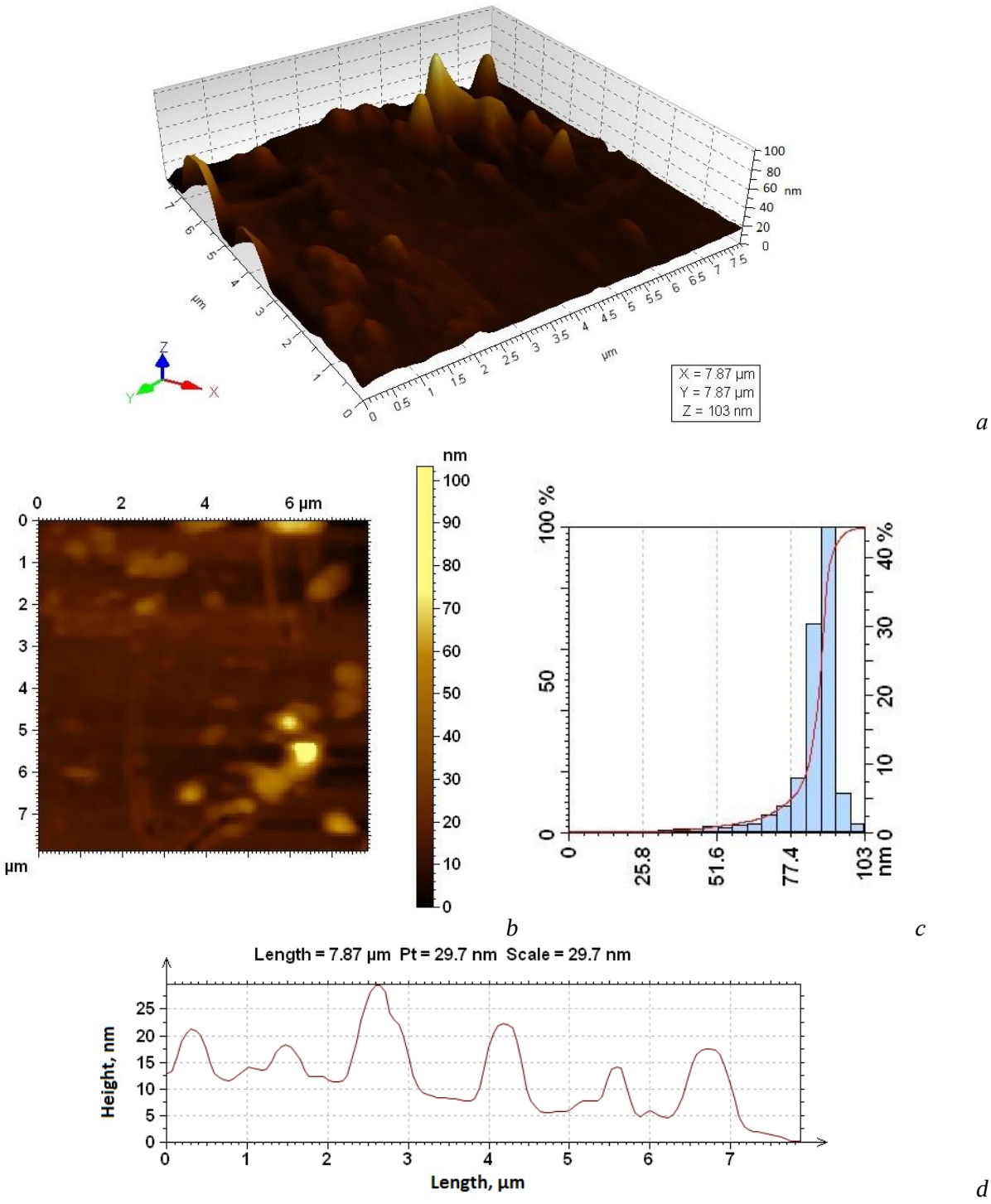

Figure 7. AFM image (*a*, *b*), distribution histogram (*c*), and surface relief (*d*) of the film of sample S-4 (in the presence of $NaBH_4/C_6H_8O_6$)

In general, the results of the AFM study indicate that the nature, amount, and presence of co-reducing agents in the formation of manganese nanoparticles in a chitosan matrix affect the formation of different morphologies. In particular, it was found that the reduction of Mn^{2+} in the presence of $NaBH_4$ resulted in cubic, tetragonal, widely spaced, densely packed nanoparticles, while the reduction in the presence of $NaBH_4/C_6H_8O_6$ resulted in mainly spherical, short-spaced, granular nanoparticles.

SEM Analysis

SEM examination of the chitosan matrix reveals a heterogeneous and non-uniform surface morphology with the presence of porous structures in the resulting films. The observed structures are distributed on the micron scale; however, it should be noted that SEM provides mainly qualitative information on the surface morphology. Therefore, the observed porous structures are discussed in terms of morphological heterogeneity rather than as a quantitative measure of porosity. Such surface characteristics are consistent with the amorphous nature of chitosan and its tendency to form irregular, loosely packed structures upon drying of the films (Fig. 8). Such morphological behavior has been widely described for chitosan-based systems and is known to promote interactions with metal ions and contribute to the stabilization and morphological control of nanoparticles [45, 52].

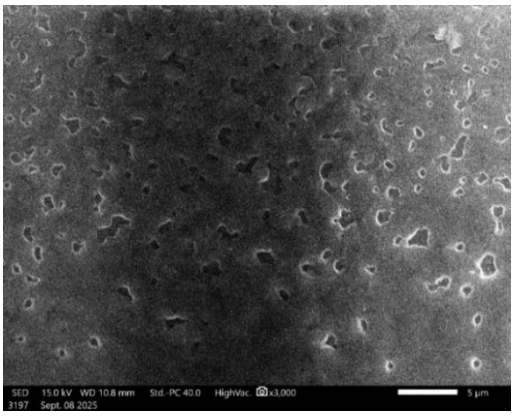

Figure 8. SEM image of the CS sample

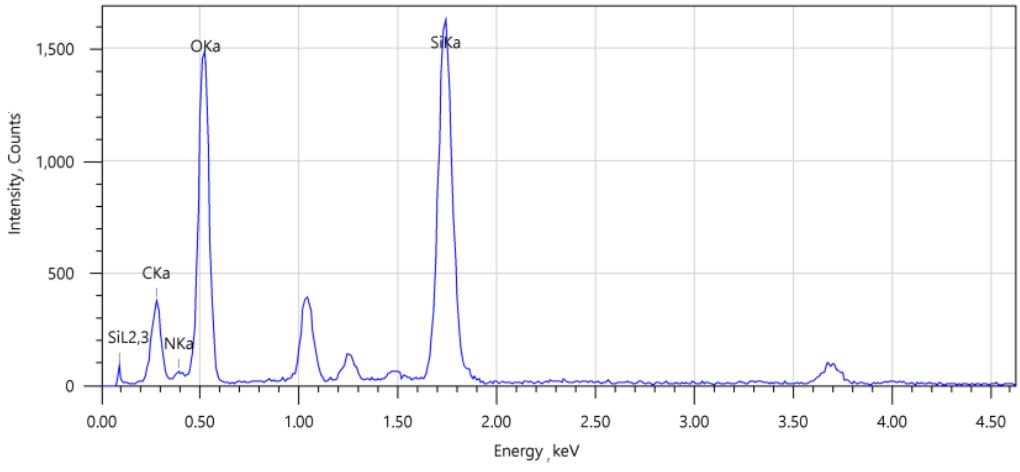

a

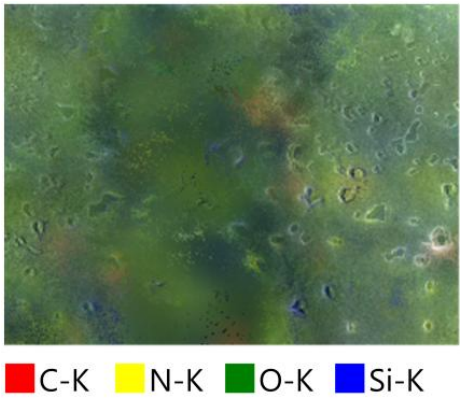

b

Figure 9. Energy dispersive spectroscopic (EDS) analysis of chitosan (*a*) and EDS element distribution map (*b*)

According to the results of energy dispersive analysis, the chitosan sample was found to contain mainly C, N, and O elements. The elemental composition analysis revealed a large proportion of Si (23 wt%) and O (41 wt%), which is explained by the fact that the sample was tested on a SiO_2-based glass substrate. It was also confirmed that chitosan itself contains 27 wt% C and a small amount of N (Fig. 9).

According to the SEM results, it was found that the chitosan-stabilized Mn nanoparticles constituting the S-3 sample were mainly formed in cubic and tetragonal shapes. Since the samples were observed in a film state, the formed particles in it grew and agglomerated in certain areas. In general, the size of the nanoparticles ranged from 100 nm to 800 nm (Fig. 10).

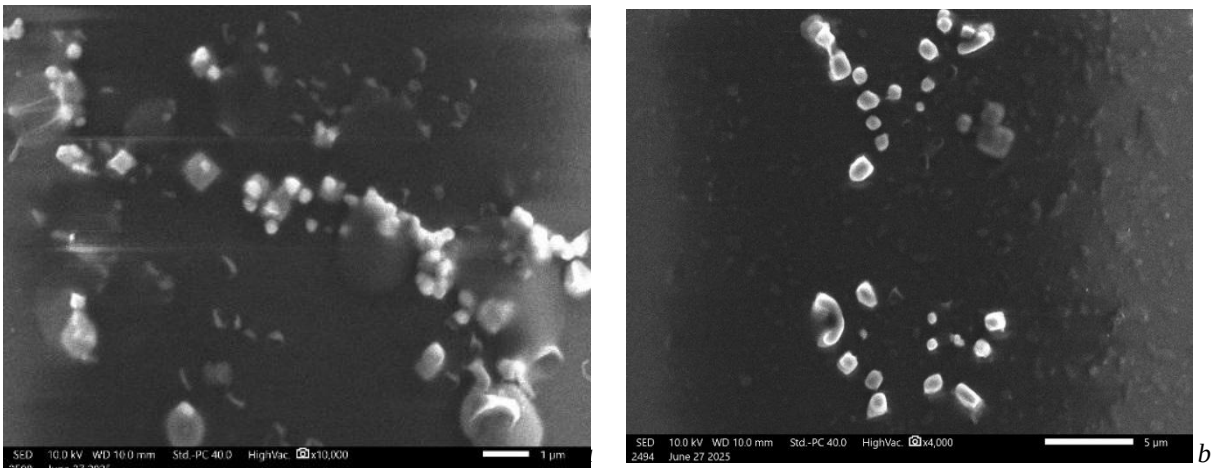

b

Figure 10. SEM micrographs of sample S-3: (*a*) 1 µm scale bar; (*b*) 5 µm scale bar

The formation of nanoparticles with different structures mainly depends on the reducing potential of the reducing agents and the chemical nature of the reaction medium, which control the nucleation and growth mechanisms of particles in a certain direction during the synthesis process. As a result, the formation of nanoparticles with different morphology and crystal structure is observed in the nanosystems formed by the chemical reduction reaction of Mn^{2+} ions in the presence of $NaBH_4$ and $NaBH_4/C_6H_8O_6$ in a chitosan medium. The formation of the morphology of the S-3 sample affects the growth and formation of particles in the process of chitosan as a matrix, but there is no additional antioxidant or complex-forming effect. As a result, a low-energy and crystallized tetragonal crystal structure is formed [74].

The EDS mapping results of the S-3 sample show that the nanoparticles contain carbon (C), nitrogen (N), oxygen (O) and manganese (Mn). This indicates a high level of salinity. The EDS spectrum of the S-3 sample shows a carbon content of 10.17 wt.%, as well as a very small amount of nitrogen and 12.8 wt.% manganese (Fig. 11).

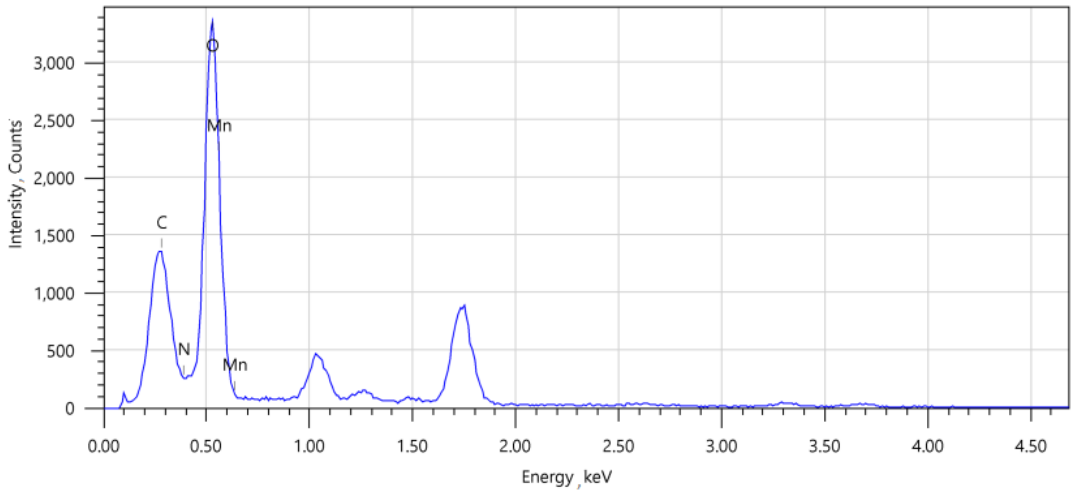

a

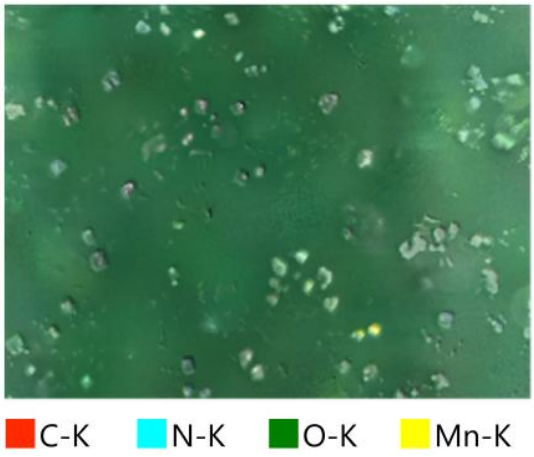

b

Figure 11. Energy dispersive spectroscopic (EDS) analysis (*a*) and element distribution map (*b*) of sample S-3

SEM analysis of the S-4 sample showed that the nanoparticles were mainly spherical in shape, with the size of the nanoparticles ranging from 500 to 750 nm (Fig. 12). In the S-4 sample (Mn^{2+}/$NaBH_4$/$C_6H_8O_6$/–CS), the reaction with manganese ions complexed with chitosan controls the growth and aggregation of the particles. Nanoparticles form predominantly spherical aggregated structures, energetically favorable due to their symmetrical geometry. The presence of ascorbic acid reduces excessive cross-linking during the interaction of manganese compounds with chitosan, thereby promoting the formation of more compact and symmetrical low-energy aggregates. However, the spherical formations observed in SEM images correspond to aggregated particles, not individual primary nanoparticles, and therefore cannot be considered direct evidence of the shapes of individual particles. Accordingly, the effect of ascorbic acid is manifested primarily through its influence on the reduction process and interparticle interactions that determine the aggregation behavior of the system, rather than through the formation of clearly defined shapes of the primary nanoparticles [75, 76].

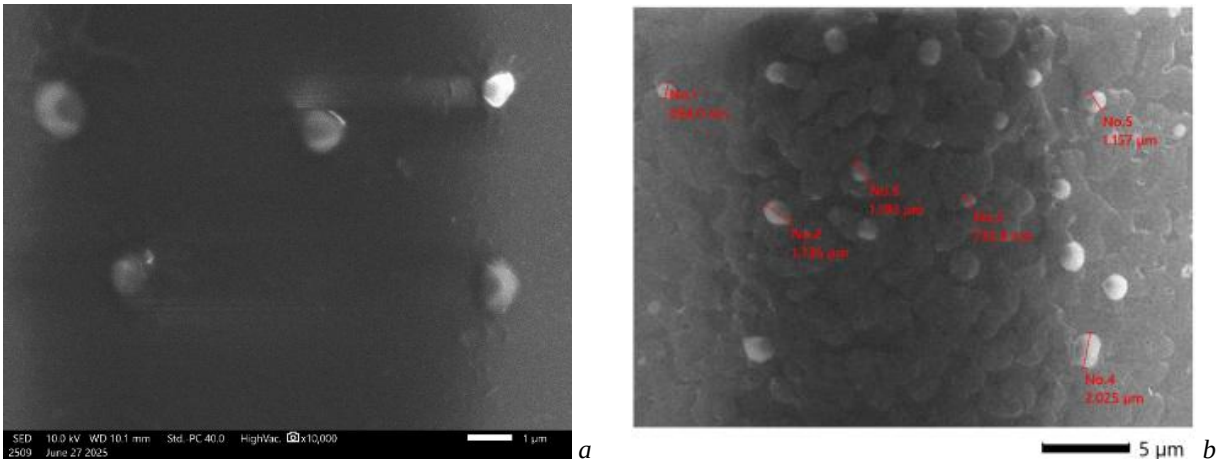

a *b*

Figure 12. SEM micrographs of sample S-4: (*a*) 1 µm scale bar; (*b*) 5 µm scale bar

The EDS mapping results of the S-4 sample indicate that the nanoparticles contain carbon (C), nitrogen (N), oxygen (O), and manganese (Mn). The EDS spectrum of the S-4 sample shows a carbon content of 13.7 wt.%, as well as a very small amount of nitrogen and 11.3 wt.% manganese (Fig. 13).

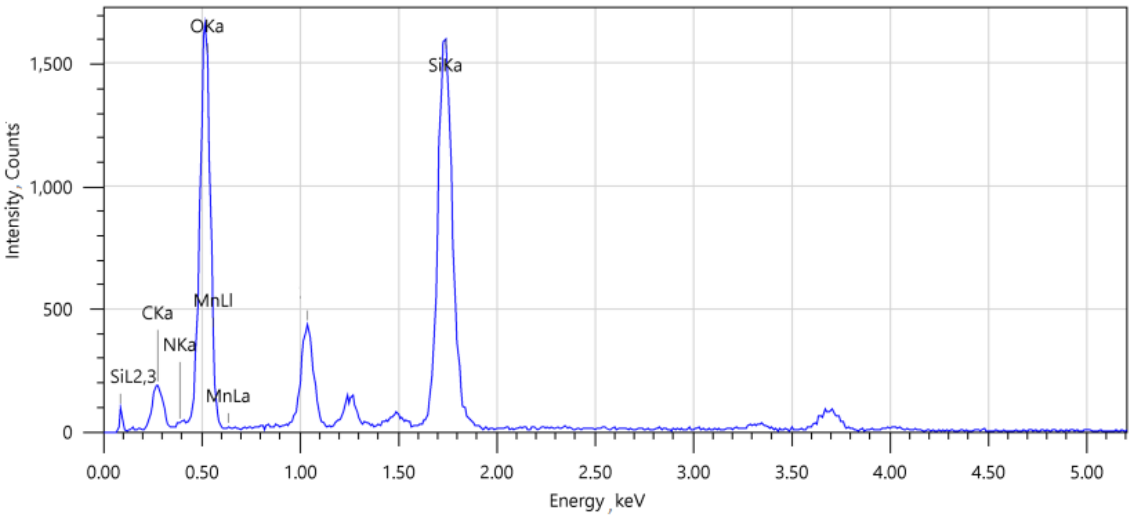

a

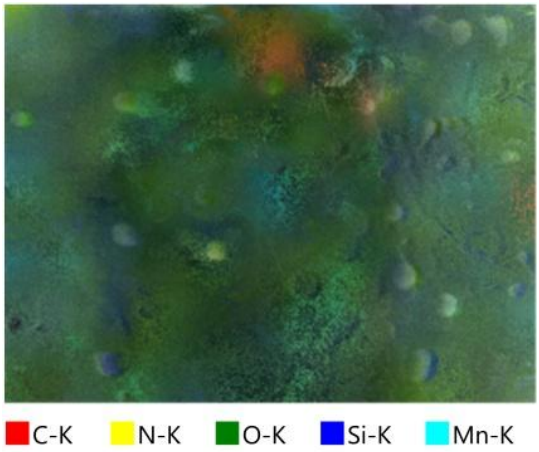

b

Figure 13. Energy dispersive spectroscopic (EDS) analysis (*a*) and element distribution map (*b*) of sample S-4

The nanoparticle of manganese is currently poorly studied in the literature, and most studies have focused on analyzing the nanostructures of its hybrid and composite forms. In particular, nanoparticles based on manganese ferrite ($MnFe_2O_4$) with chitosan have formed spherical [77–79], hillock, rod and sheet structures with $ZnMn_2O_4$ [77], patch-shaped structures with carbon nanofibers of Mn [80], spherical structures with $Mn_{0.8}Zn_{0.2}Fe_2O_4$ with chitosan [81], and spherical structures with chitosan–Mn complexes in liquid [82]. Manganese nanoparticles were present in various composites, including ferrite, metal, hybrid, and complex forms, and were mainly observed in spherical, rod-shaped, or lamellar morphologies, with sizes in the 10–150 nm range. In all cases, chitosan coating was found to be an important factor in improving dispersion, reducing aggregation, and enhancing bioactivity.

Comparative Analysis

The general properties of manganese nanoparticles synthesized in the presence and absence of chitosan were comparatively analyzed (Table 2). In the control samples synthesized in the absence of chitosan (S-1 and S-2), the particles exhibited a pronounced tendency toward aggregation. DLS analysis revealed that their size distribution was predominantly in the micrometer range (6–12 μm), while SEM images showed large particles with irregular morphology. On the contrary, in the samples obtained in the presence of chitosan (S-3, S-4), the hydrodynamic dimensions were determined in the range of 300–500 nm, and the morphology was manifested in cubic and spherical shapes in SEM analysis, and dense and ordered particles in the range of 50–100 nm were observed in AFM studies.

Table 2

Composition and structural characteristics of manganese particles formed with and without chitosan

№	Sample	Mass of Mn, mg	Mass of CS, mg	DLS nm/μm	SEM results	AFM results	EDS Mn (%) → Mn content: 0.5–1.0 wt%	Explanation
1	S-1 (control)	1.32	–	10–12 μm (aggregated)	–	–	–	Rapid nucleation and enlargement
2	S-2 (control)	1.32	–	6–8 μm (aggregated)	–	–	–	Ascorbic acid controlled growth, but large
3	S-3 (*in situ*)	1.32	60	300–500 nm	Cubic, tetragonal, 100–800 nm (aggregates)	50 ± 10 nm	12.8 % → 0.128 g	Colloidal stability is high
4	S-4 (*in situ*)	1.32	60	300–500 nm	Spherical, 500–750 nm	90 ± 20 nm	11.3 % → 0.113 g	Symmetric sphere morphology
5	Mn biological requirement (daily)	2–5 mg [83]	–	50–300 [23, 31]	Mn is spherical or cubic in its pure state, while CS can have spherical, cubic, rod-shaped, tetragonal, and other morphologies; 10–800 [45, 52]	20–250 nm [60, 67]	–	WHO/EFSA standards [83]

Note: DLS and AFM values are presented as average ± standard deviation based on at least three independent measurements. SEM data are given as size ranges due to aggregation effects. EDS values are semi-quantitative with an estimated instrumental error of ±1 wt%.

According to EDS data, the mass fraction of manganese in the chitosan matrix is 11–13 %, which corresponds to 0.113–0.128 g of Mn per gram of sample. These values are quite small in nanoscale when compared with the recommended daily intake for humans (2–5 mg), and are of great importance from the point of view of biological safety. Thus, the results presented in the table clearly demonstrate the effectiveness of chitosan in stabilizing manganese nanoparticles and their morphological and physicochemical advantages.

Conclusions

In conclusion, Manganese-containing nanoparticles were successfully synthesized in the presence of *Bombyx mori* chitosan using $NaBH_4$ and $NaBH_4/C_6H_8O_6$ as reducing systems under controlled *in situ* conditions. Dynamic light scattering analysis demonstrated the formation of stable nanosystems with hydrodynamic sizes of 118–144 nm and narrow dominant distributions (96-97 %), indicating effective stabilization by the polymer matrix. IR spectroscopic analysis confirmed structural rearrangements within the chitosan framework and the involvement of –NH and –C=O functional groups in nanoparticle binding, supporting a chemisorption-based stabilization mechanism. X-ray diffraction results verified the reduction of Mn^{2+} ions and revealed the presence of crystalline phases, while also indicating partial oxidation during nanoparticle formation.

SEM and AFM analyses showed well-dispersed metal nanoparticles embedded in the chitosan matrix, with predominant sizes of approximately 50 nm (tetragonal) and 90 nm (spherical), confirming morphology control under the selected synthesis parameters. Surface topology studies further demonstrated uniform particle distribution without large-scale aggregation. Overall, the combined structural and morphological analyses confirm that chitosan effectively regulates nucleation, growth, and stabilization of manganese nanoparticles. Thus, the resulting manganese-containing nanosystems are of interest for their application in veterinary medicine.

Funding

This study was conducted with the basic funding of the Academy of Sciences of the Republic of Uzbekistan.

*Author Information**

**The authors' names are presented in the following order: First Name, Middle Name and Last Name*

Kandiyor Khorun ogli Ergashev (*corresponding author*) — PhD, Junior Researcher, Institute of Polymer Chemistry and Physics; National Pedagogical University of Uzbekistan, 100128, Tashkent, Uzbekistan; e-mail: kandiyor_ergashev@yahoo.com; https://orcid.org/0000-0001-7494-5988

Noira Rakhimovna Vokhidova — Doctor of Chemical Sciences, Professor, Head of the Laboratory of Interpolyelectrolyte Complexes and Metallopolymers, Institute of Polymer Chemistry and Physics, 100128, Tashkent, Uzbekistan; e-mail: noira_vokhidova@yahoo.de; https://orcid.org/0000-0003-0477-3708

Sayyora Sharafovna Rashidova — Doctor of Chemical Sciences, Professor, Academician, Consultant of the Director, Institute of Polymer Chemistry and Physics, 100128, Tashkent, Uzbekistan; e-mail: polymer@academy.uz; https://orcid.org/0000-0003-1667-4619

Author Contributions

The manuscript was written through contributions of all authors. All authors have given approval to the final version of the manuscript. CRediT: **Ergashev Kandiyor Khorun ogli** investigation, validation, writing-original draft; formal analysis, editing; **Vokhidova Noira Rakhimovna** conceptualization, data curation, formal analysis, validation, writing-review & editing; **Sayyora Sharafovna Rashidova** conceptualization, supervision, editing.

Acknowledgments

Figure 1 and Graphical Abstract were created in *BioRender. Ergashev, Q. (2026) https://BioRender.com/qy5h0tq*

Conflict of Interest

The authors declare no conflict of interest

References

1 Tunc, O., Thompson, J., & Tremellen, K. (2010). Development of the NBT assay as a marker of sperm oxidative stress. *International Journal of Andrology*, *33*(1), 13–21. https://doi.org/10.1111/j.1365-2605.2008.00941.x

2 Horning, K. J., Caito, S. W., Tipps, K. G., Bowman, A. B., & Aschner, M. (2015). Manganese is essential for neuronal health. *Annual Review of Nutrition*, *35*, 71–108. https://doi.org/10.1146/annurev-nutr-071714-034419

3 Dorman, D.C., Struve, M.F., James, R.A., McManus, B.E., Marshall, M.W., & Wong, B.A. (2001). Influence of dietary manganese on the pharmacokinetics of inhaled manganese sulfate in male CD rats. *Toxicological Sciences*, *60*(2), 242–251. https://doi.org/10.1093/toxsci/60.2.242

4 Grujicic, J., & Allen, A.R. (2025). Manganese superoxide dismutase: Structure, function, and implications in human disease. *Antioxidants*, *14*(7), 848. https://doi.org/10.3390/antiox14070848

5 Studer, J. M., Schweer, W. P., Gabler, N. K., & Ross, J. W. (2022). Functions of manganese in reproduction. *Animal Reproduction Science*, *238*, Article 106924. https://doi.org/10.1016/j.anireprosci.2022.106924

6 Cheema, R. S., Bansal, A. K., Bilaspuri, G. S. (2009). Manganese provides antioxidant protection for sperm cryopreservation that may improve fertilizing ability of buffalo (*Bubalus bubalis*) spermatozoa. *Oxidative Medicine and Cellular Longevity*, *2*(3), 152–159. https://doi.org/10.4161/oxim.2.3.8804

7 De Pascali, F., Tréfier, A., Landomiel, F., Bozon, V., Bruneau, G., Yvinec, R., Poupon, A., Crépieux, P., & Reiter, E. (2018). Follicle-stimulating hormone receptor: Advances and remaining challenges. *International Review of Cell and Molecular Biology*, *338*, 1–58. https://doi.org/10.1016/bs.ircmb.2018.02.001

8 Lee, B., Pine, M., Johnson, L., Rettori, V., Hiney, J. K., & Dees, W.L. (2006). Manganese acts centrally to activate reproductive hormone secretion and pubertal development in male rats. *Reproductive Toxicology*, *22*(4), 580–585. https://doi.org/10.1016/j.reprotox.2006.03.011

9 Yang, H., Wang, J., Yang, X., Wu, F., Qi, Z., Xu, B., Liu, W., & Deng, Y. (2019). Occupational manganese exposure, reproductive hormones, and semen quality in male workers: A cross-sectional study. *Toxicology and Industrial Health*, *35*(1), 53–62. https://doi.org/10.1177/0748233718810109

10 Kim, E. A., Cheong, H. -K., Joo, K.-D., Shin, J.-H., Lee, J. S., Choi, S.-B., Kim, M.-O., Lee, I. J., & Kang, D. M. (2007). Effect of manganese exposure on the neuroendocrine system in welders. *NeuroToxicology*, *28*(2), 263–269. https://doi.org/10.1016/j.neuro.2006.07.013

11 Roy, T., Boateng, S. T., Uddin, M. B., Banang-Mbeumi, S., Yadav, R. K., Bock, C. R., Folahan, J. T., Siwe-Noundou, X., Walker, A. L., King, J. A., Buerger, C., Huang, S., & Chamcheu, J. C. (2023).The PI3K-Akt-mTOR and associated signaling path-

ways as molecular drivers of immune-mediated inflammatory skin diseases: Update on therapeutic strategy using natural and synthetic compounds. *Cells, 12*(12), 1671. https://doi.org/10.3390/cells12121671

12 Srivastava, V. K., Hiney, J. K., Dees, W. L. (2013). Early life manganese exposure upregulates tumor-associated genes in the hypothalamus of female rats: relationship to manganese-induced precocious puberty. *Toxicological Sciences, 136*(2), 373–381. https://doi.org/10.1093/toxsci/kft195

13 Tinkov, A. A., Paoliello, M. M. B., Mazilina, A. N., Skalny, A. V., Martins, A. C., Voskresenskaya, O. N., Aaseth, J., Santamaria, A., Notova, S. V., Tsatsakis, A., Lee, E., Bowman, A. B., & Aschner, M. (2021). Molecular targets of manganese-induced neurotoxicity: A five-year update. *International Journal of Molecular Sciences, 22*(9), 4646. https://doi.org/10.3390/ijms22094646

14 Peng, Y., & He, Q. (2024). Reproductive toxicity and related mechanisms of micro(nano)plastics in terrestrial mammals: Review of current evidence. *Ecotoxicology and Environmental Safety, 279*, 116505. https://doi.org/10.1016/j.ecoenv.2024.116505.

15 da Silva, J. D. O., dos Santos, H. C., Bento, G. S., Oliveira, J. F. R., Abud, A. K. S., & Gimenez, I. de F. (2024). Green synthesis of manganese dioxide (MnO_2) nanoparticles produced with acerola (*Malpighia emarginata*) leaf extract. *Materials Chemistry and Physics, 315*, 128963. https://doi.org/10.1016/j.matchemphys.2024.128963

16 Tazim, T. Q., Kawsar, M., Hossain, M. S., Bahadur, N. M., & Ahmed, S. (2025). Hydrothermal synthesis of nano-metal oxides for structural modification: A review. *Next Nanotechnology, 7*, 100167. https://doi.org/10.1016/j.nxnano.2025.100167

17 Huo, Y., Xiu, S., Meng, L.-Y., & Quan, B. (2023). Solvothermal synthesis and applications of micro/nano carbons: A review. *Chemical Engineering Journal, 45*1, 138572. https://doi.org/10.1016/j.cej.2022.138572

18 Kirubakaran, D., Wahid, J. B. A., Karmegam, N., Jeevika, R., Sellapillai, L., Rajkumar, M., & SenthilKumar, K.J. (2025). A comprehensive review on the green synthesis of nanoparticles: Advancements in biomedical and environmental applications. *Biomedical Materials & Devices, 4*, 388–413. https://doi.org/10.1007/s44174-025-00295-4

19 Chaschin, I. S., Perepelkin, E. I., Levin, E. E., Abramchuk, S. S., Anuchina, N. M., Kizas, O. A., Ryzhova, Y. V., & Bakuleva, N. P. (2025). Green synthesis of silver nanoparticles using chitosan in carbonic acid solutions: Effect of pressure and temperature on the structure and antimicrobial properties. *Journal of Inorganic and Organometallic Polymers and Materials, 35*, 2287–2299. https://doi.org/10.1007/s10904-024-03212-2

20 Kustov, L., & Vikanova, K. (2023). Synthesis of metal nanoparticles under microwave irradiation: Get much with less energy. *Metals, 13*(10), 1714. https://doi.org/10.3390/met13101714

21 Karadi, I., Hiremath, V. J., & Timmanagoudar, S. (2025). Nano ferrites: Synthesis, properties and emerging applications — A comprehensive review. *Journal of Advancements in Material Engineering, 10*(2), 1–21. https://doi.org/10.46610/JoAME.2025.v10i02.001

22 Zhang, X., Sathiyaseelan, A., Naveen, K. V., Lu, Y., & Wang, M.-H. (2023). Research progress in green synthesis of manganese and manganese oxide nanoparticles in biomedical and environmental applications — A review. *Chemosphere, 337*, 139312. https://doi.org/10.1016/j.chemosphere.2023.139312

23 Luo, Z. C., Cui, Y. X., Liu, Z. X., Liu, T. L., Yin, F. X., & Zheng, K. H. (2024). Oxidation mechanism of high-manganese heat-resistant steels reinforced by *in situ* second-phase particles. *Corrosion Science, 227*, 111720. https://doi.org/10.1016/j.corsci.2023.111720

24 Li, K., Li, H., Xiao, T., & Zhang, G. (2020). Zero-valent manganese nanoparticles coupled with different strong oxidants for thallium removal from wastewater. *Frontiers of Environmental Science & Engineering, 14*(2). https://doi.org/10.1007/s11783-019-1213-5

25 Akduman, H. Ö., & Özdemir, E. (2025). Zirconia supported bimetallic Co–Mn–B catalyst with superior catalytic activity for hydrolysis of sodium borohydride. *International Journal of Hydrogen Energy, 100*, 67–78. https://doi.org/10.1016/j.ijhydene.2024.12.261

26 Szczyglewska, P., Feliczak-Guzik, A., & Nowak, I. (2023). Nanotechnology–General aspects: A chemical reduction approach to the synthesis of nanoparticles. *Molecules, 28*(13), 4932. https://doi.org/10.3390/molecules28134932

27 Ullah, R., & Dutta, J. (2008). Photocatalytic degradation of organic dyes with manganese-doped ZnO nanoparticles. *Journal of Hazardous Materials, 156*(1–3), 194–200. https://doi.org/10.1016/j.jhazmat.2007.12.033

28 Bao, C., Serrano-Lotina, A., Niu, M., Portela, R., Li, Y., Lim, K. H., Liu, P., Wang, W. -j., Bañares, M. A., & Wang, Q. (2023). Microwave-associated chemistry in environmental catalysis for air pollution remediation: A review. *Chemical Engineering Journal, 466*, 142902. https://doi.org/10.1016/j.cej.2023.142902

29 Zenner, J., Tran, K., Kang, L., Kinzel, N. W., Werlé, C., DeBeer, S., Bordet, A., & Leitner, W. (2024). Synthesis, Characterization, and Catalytic Application of Colloidal and Supported Manganese Nanoparticles. *Chemistry — A European Journal, 30*, e202304228. https://doi.org/10.1002/chem.202304228

30 Trofimova, O. Y., Ershova, I. V., Maleeva, A. V., et al. (2024). Synthesis and Properties of Manganese(II) and Nickel(II) 1-D Coordination Polymers Based on 2,5-di-hydroxy-3,6-di-tert-butyl-para-quinone. *Journal of Inorganic and Organometallic Polymers and Materials, 34*, 2779–2787. https://doi.org/10.1007/s10904-024-03013-7

31 Xu, Z., Zhao, W., Liu, J., Fan, J. (2023). Research on the Surfactant-Assisted Synthesis of MnZn Ferrite Precursor Powders. *Magnetochemistry, 9*(6), 146. https://doi.org/10.3390/magnetochemistry9060146

32 Wang, W., Ding, Z., Zhao, X., Wu, S., Li, F., Yue, M., & Liu, J. P. (2015). Microstructure and magnetic properties of MFe_2O_4 (M = Co, Ni, and Mn) ferrite nanocrystals prepared using colloid mill and hydrothermal method. *Journal of Applied Physics, 117*(17), 17A328. https://doi.org/10.1063/1.4917463

33 Hu, M., Yan, X., Hu, X., Feng, R., & Zhou, M. (2019). Synthesis of silver decorated silica nanoparticles with rough surfaces as adsorbent and catalyst for methylene blue removal. *Journal of Sol-Gel Science and Technology, 89*(3), https://doi.org/10.1007/s10971-018-4871-z

34 Rostami, S., Mehdinia, A., & Jabbari, A. (2017). Seed-mediated grown silver nanoparticles as a colorimetric sensor for detection of ascorbic acid. *Spectrochimica Acta Part A: Molecular and Biomolecular Spectroscopy, 180*, 204–210. https://doi.org/10.1016/j.saa.2017.03.020

35 Varin, R. A., Mattar, D. K., Bidabadi, A. S., & Polański, M. K. (2017). Synthesis of amorphous manganese borohydride in the ($NaBH_4$–$MnCl_2$) system, its hydrogen generation properties and crystalline transformation during solvent extraction. *Journal of Energy Chemistry, 26*(1), 24–34. http://dx.doi.org/10.1016/j.jechem.2016.08.011

36 Wang, M., Pang, P., Koopal, L. K., Suib, S.; Wang, Y., & Liu, F. (2014). One-step synthesis of δ-MnO_2 nanoparticles using ascorbic acid and their scavenging properties to Pb(II), Zn(II) and methylene blue. *Materials Chemistry and Physics, 148*(3), 1149–1156. https://doi.org/10.1016/j.matchemphys.2014.09.037

37 Siddique, M. A. R., Khan, M. A., Bokhari, S. A. I., Ismail, M., Ahmad, K., Haseeb, H. A., Kayani, M. M., Khan, S., Zahid, N., & Khan, S.B. (2024). Ascorbic acid-mediated selenium nanoparticles as potential antihyperuricemic, antioxidant, anticoagulant, and thrombolytic agents. *Green Processing and Synthesis, 13*, 20230158. https://doi.org/10.1515/gps-2023-0158

38 Patra, S. K., Molla, M. R., Singh, A. K., Ghosh, P. K., & Jana, R. N. (2021). Synthesis and purification of metal nanoparticles by membrane filtration. *Journal of Inorganic and Organometallic Polymers and Materials, 31*(4), 1357–1366. https://doi.org/10.1007/s10904-021-01927-3

39 Alam, M. A., Ahmed, S., Bishwas, R. K., Mostofa, S., & Jahan, S. A. (2025). X-ray crystallographic diffraction study by whole powder pattern fitting (WPPF) method: Refinement of crystalline nanostructure polymorphs TiO_2. *South African Journal of Chemical Engineering, 51*, 68–77. https://doi.org/10.1016/j.sajce.2024.10.010

40 Ben Amor, I., Hemmami, H., Grara, N., Aidat, O., Ben Amor, A., Zeghoud, S., & Bellucci, S. (2024). Chitosan: A Green Approach to Metallic Nanoparticle/Nanocomposite Synthesis and Applications. *Polymers, 16*(18), 2662. https://doi.org/10.3390/polym16182662

41 Eltaweil, A. S., El-Tawil, A. M., Abd El-Monaem, E. M., & El-Subruiti, G. M. (2021). Zero Valent Iron Nanoparticle-Loaded Nanobentonite Intercalated Carboxymethyl Chitosan for Efficient Removal of Both Anionic and Cationic Dyes. *ACS Omega, 6*(9), 6348–6360. https://doi.org/10.1021/acsomega.0c06251

42 Rinaudo, M. (2006). Chitin and chitosan: Properties and applications. *Progress in Polymer Science, 31*(7), 603–632. https://doi.org/10.1016/j.progpolymsci.2006.06.001

43 Sajna, P., Varma, A., & Vasudevan, G. (2008). Application of Spectroscopic Methods for Structural Analysis of Chitin and Chitosan. *Marine Drugs, 8*(5), 1567–1587. https://doi.org/10.3390/md8051567

44 Hu, Z., Lu, S., Cheng, Y., Kong, S., Li, S., Li, C., & Yang, L. (2019). Investigation of the effects of molecular parameters on the hemostatic properties of chitosan. *International Journal of Biological Macromolecules, 136*, 327–336. https://doi.org/10.3390/molecules23123147

45 Wang, Y., Chen, X., Liu, J., Zhang, L., & Zhao, X. (2021). Synthesis of chitosan–metal nanocomposites for biomedical applications. *Materials Science and Engineering: C, 124*, 112051. https://doi.org/10.1016/j.msec.2021.112051

46 Filippov, S. K., Khusnutdinov, R., Murmiliuk, A., Inam, W., Zakharova, L. Ya., Zhang, H., & Khutoryanskiy, V. V. (2023). Dynamic light scattering and transmission electron microscopy in drug delivery: A roadmap for correct characterization of nanoparticles and interpretation of results. *Materials Horizons, 10*, 5354–5370. https://doi.org/10.1039/d3mh00717k

47 Kim, S. et al. (2020). Structural insights into chitosan–ZnO nanocomposites using FTIR and XRD. *Journal of Molecular Structure, 1212*, 128118. https://doi.org/10.1016/j.molstruc.2020.128118

48 Faizan, M., Naz, M. Y., Shah, S. A. S. A., Shakir, I., Khaliq, M., Busharat, M. A., & Pan, D. (2025). Mesoporous magnetic $MnFe_2O_4$@SiO_2-chitosan nanocomposite for efficient adsorptive removal of Zn(II) and Cd(II) ions from aqueous media. *Desalination and Water Treatment, 324*, 101488. https://doi.org/10.1016/j.dwt.2025.101488

49 Rodrigues de Sá, M., Mendes da Silva, T., Souza, E.S., Soares de Carvalho, A., Filho, M. R. A. A., Silva-Araújo, E. R. (2025). Magnetic and fluorescent manganese silicate nanostructures for advanced applications. *ChemistrySelect, 10*(24), e02098. https://doi.org/10.1002/slct.202502098

50 Kumar, S., Yadav, B., Sharma, P., Singh, R., & Gupta, A. (2021). Preparation and Characterization of Chitosan-Coated Manganese Ferrospinel Nanoparticles Conjugated with Laccase for Environmental Bioremediation. *Polymers, 13*(22), 3921. https://doi.org/10.3390/polym13223921

51 Lahouti, S., & Naeimi, H. (2020). Chitosan-encapsulated manganese ferrite particles bearing sulfonic acid group catalyzed efficient synthesis of spiro indenoquinoxalines. *RSC Advances, 10*(55), 33334–33343. https://doi.org/10.1039/d0ra04925e

52 Nguyen, T. V., Le, H. T., Pham, H. T., & Nguyen, D. T. (2023). Chitosan based nanosorbents for removal of heavy metals: Cd, Co, Cu, and Pb. *Scientific Reports, 13*, Article 16958. https://doi.org/10.1038/s41598-023-44014-5

53 Patel, R., Mehta, A., & Joshi, M. (2018). Synthesis of $MnFe_2O_4$@chitosan nanocomposites for magnetic hyperthermia and drug delivery applications. *Materials, 11*(12), 2542. https://doi.org/10.3390/ma11122542

54 Zhang, Q., Liu, J., Wang, X., Li, Y., & Chen, H. (2021). Catalytic application of Pd–Chitosan@$MnFe_2O_4$ nanocomposites: Structure and interaction analysis. *Journal of Molecular Liquids, 339*, 117222. https://doi.org/10.1016/j.molliq.2021.117222

55 Goy, R. C., de Britto, D., & Assis, O. B. G. (2009). A review of the antimicrobial activity of chitosan. *Polímeros, 19*(3), 241–247. https://doi.org/10.1590/S0104-14282009000300006

56 Niu, Y., Hu, W. (2024). Preparation, characterization and application in environmental protection of low-molecular-weight chitosan: a review. *Sustain Environ Res 34*, 29. https://doi.org/10.1186/s42834-024-00236-8

57 Podgorbunskikh, E., Kuskov, T., Rychkov, D., Lomovskii, O., & Bychkov, A. (2022). Mechanical amorphization of chitosan with different molecular weights. *Polymers, 14*(20), 4438. https://doi.org/10.3390/polym14204438

58 Lawson, A. C., Vandervoort, K. G., Welp, U., & Hinks, D.G. (1994). Magnetic structure of α-manganese. *Journal of Applied Physics, 76*(10), 7049–7051. https://doi.org/10.1063/1.358261

59 Yamauchi, H., Sari, D. P., Watanabe, I., & Yasui, Y. (2020). High-temperature short-range order in Mn_3RhSi. *Communications Materials, 1*, 43. https://doi.org/10.1038/s43246-020-0042-1

60 Pardeep, Bitla, Y., Lalita, Patra, A. K., & Basheed, G. A. (2023). In-field critical behaviour of β-Mn type Co–Zn–Mn skyrmion-host. *Physica B: Condensed Matter, 654*, 414669. https://doi.org/10.1016/j.physb.2023.414669

61 Hornfeck, W., & Kuhn, P. (2014). Octagonal symmetry in low-discrepancy β-manganese. *Acta Crystallographica Section A Foundations and Advances, 70*(5), 441–447. https://doi.org/10.1107/s2053273314009218

62 Karube, K., White, J. S., Ukleev, V., Dewhurst, C. D., Cubitt, R., Kikkawa, A., Tokunaga, Y., Rønnow, H. M., Tokura, Y., & Taguchi, Y. (2020). Metastable skyrmion lattices governed by magnetic disorder and anisotropy in β-Mn-type chiral magnets. *Physical Review B, 102*(6), 064408. https://doi.org/10.1103/PhysRevB.102.064408

63 Bakshi, P. S., Singha, M., & Rathi, P. (2013). Structural modification in chitosan after metal oxide incorporation: An XRD analysis. *Carbohydrate Polymers, 98*, 599–606. https://doi.org/10.1016/j.carbpol.2013.07.083

64 Wang, X., Chen, X., Zhang, Y., Li, Y., & Zhao, J. (2015). Synthesis and characterization of Mn nanoparticles via reduction of $MnCl_2$. *Journal of Alloys and Compounds, 648*, 837–843. https://doi.org/10.1016/j.jallcom.2015.07.164

65 Rasaee, M. J., Esfandiari, M., Soleimani, M., Azimi, S., & Fazeli, M. (2022). Structural and antimicrobial properties of chitosan‐based nanoparticles. *Polymers, 14*(24), 5324. https://doi.org/10.3390/polym14245324

66 Shoemaker, C. B., Shoemaker, D. P., Hopkins, T. E., & Yindepit, S. (1978). Refinement of the structure of β-manganese and of a related phase in the Mn–Ni–Si system. *Acta Crystallographica Section B Structural Crystallography and Crystal Chemistry, 34*(12), 3573–3576. https://doi.org/10.1107/s0567740878011620

67 Pandey, R., & Shukla, S. (2023). Nanocomposites of chitosan with transition metals: synthesis and physicochemical properties. *Materials Chemistry and Physics, 303*, 127596. https://doi.org/10.1016/j.matchemphys.2023.127596

68 Liu, Y., Zhang, X., Li, J., & Wang, S. (2021). Structural properties of chitosan‐based nanocomposites with transition metals. *Polymers, 13*(16), 2714. https://doi.org/10.3390/polym13162714

69 Zhuo, Shujuan; Fang, Jing; Li, Meng; Wang, Jing; Zhu, & Changqing; Du, Jinyan (2019). Manganese(II)-doped carbon dots as effective oxidase mimics for sensitive colorimetric determination of ascorbic acid. *Microchimica Acta, 186* (745). https://doi.org/10.1007/s00604-019-3887-6

70 Deshmukh, Aarti R., & Kim, Beom Soo. (2019). Chitosan–Vitamin C Nanoparticles. *KSBB Journal, 34* (4), 221–232. https://doi.org/10.7841/ksbbj.2019.34.4.221

71 Podgorbunskikh, E., et al. (2022). Mechanical Amorphization of Chitosan with Different Molecular Weights. *Polymers, 14*(20), 4438. https://doi.org/10.3390/polym14204438

72 Nosal, W. H., Thompson, D. W., Yan, L., Sarkar, S., Subramanian, A., & Woollam, J. A. (2005). Infrared optical properties and AFM of spin-cast chitosan films chemically modified with 1,2 epoxy-3-phenoxy-propane. *Colloids and Surfaces B: Biointerfaces, 46*(1), 26–31. https://doi.org/10.1016/j.colsurfb.2005.08.006

73 Ferreira, A. M., et al. (2023). AFM surface characterization of chitosan films for biomedical applications. *Nanomaterials, 13*(4), 720. https://doi.org/10.3390/nano13040720

74 Li, Z., Gao, K., Han, G., Wang, R., Li, H., Zhaoabc X.S., & Guo. P. (2015). Solvothermal synthesis of $MnFe_2O_4$ colloidal nanocrystal assemblies and their magnetic and electrocatalytic properties. *New Journal of Chemistry, 39*, 361–368. https://doi.org/10.1039/C4NJ01466A

75 Wang, L., Hu, C., Nemoto, Y., Tateyama, Y., & Yamauchi, Y. (2010). On the role of ascorbic acid in the synthesis of single-crystal hyperbranched platinum nanostructures. *Crystal Growth & Design, 10*(8), 3454–3460. https://doi.org/10.1021/cg100207q

76 Elshoky, H. A., Salaheldin, T. A., Ali, M. A., & Gaber, M. H. 2018). Ascorbic acid prevents cellular uptake and improves biocompatibility of chitosan nanoparticles. *International Journal of Biological Macromolecules, 115*, 358–366. (https://doi.org/10.1016/j.ijbiomac.2018.04.055

77 Plikeva, S., Ivanov, D., Petrova, T., & Kolev, D. (2021). Preparation and characterization of chitosan-coated manganese-ferrite nanoparticles. *Polymers, 13*(9), 1453. https://doi.org/10.3390/polymers13091453

78 Ebadi, M., Asikin-Mijan, N., Jamil, M.S. Md., Iqbal, A., Yousif, E., Zain, A.R. Md, Aziz, T. H. T., & Rahimi Yusop, M. (2023). Palladium nanoparticles on chitosan coated superparamagnetic manganese ferrite. *Polymers, 15*(1), 232. https://doi.org/10.3390/polym15010232

79 Rashid, K., Ahmed, S., & Khan, M. (2020). Chitosan-encapsulated manganese ferrite bearing sulfonic acid catalyzed spiro indenoquinoxaline synthesis. *RSC Advances, 10*, 4925. https://doi.org/10.1039/D0RA04925E

80 Kumar, R., Chen, S.-M., & Lee, C.-H. (2016). Carbon nanotubes decorated with manganese nanoparticles for electrochemical determination of vitamin C. *Journal of Alloys and Compounds, 648*, 837–843. https://doi.org/10.1016/j.jallcom.2015.12.110

81 Patel, D., Singh, U., & Ghosh, S. (2023). Nanohybrid based on $Mn_{0.8}Zn_{0.2}Fe_2O_4$ functionalized with chitosan and sodium alginate for curcumin loading. *AAPS PharmSciTech*. https://doi.org/10.1208/s12249-023-02683-9

82 Davidson, E., Pereira, J., Giannelli, G. G., Murphy, Z., Anagnostopoulos, V., & Santra, S. (2023).Multi-functional chitosan nanovesicles loaded with bioactive manganese for potential wound healing applications. *Molecules, 28*(16), 6098. https://doi.org/10.3390/molecules28166098

83 Turck, D., Bohn, T., Castenmiller, J., de Henauw, S., Hirsch-Ernst, K., Knutsen, H. K., Maciuk, A., Mangelsdorf, I., McArdle, H. J., Pentieva, K., Siani, A., Thies, F., Tsabouri, S., Vinceti, M., Bornhorst, J., Cubadda, F., Dopter, A., FitzGerald, R., … Naska, A. (2023). Scientific opinion on the tolerable upper intake level for manganese. *EFSA Journal, 21*(12). https://doi.org/10.2903/j.efsa.2023.8413